Distinct broadband third-harmonic generation on a thin amorphous medium–air interface

Weimin Liu, Liang Wang, Fangyuan Han, and Chong Fang*

Department of Chemistry, Oregon State University, Corvallis, Oregon 97331, USA
*Corresponding author: Chong.Fang@oregonstate.edu

We achieve a series of distinct broadband third-harmonic generation (THG) signals at the amorphous glass–air interface attributed to third-order and cascaded third-order nonlinear processes. A novel THG laser sideband arises from cascaded interaction between fundamental pulses and the cascaded four-wave mixing signals. The spatially separated THG sidebands with distinct spectral profiles manifest femtosecond quantum beats. Using a versatile setup with two crossing near-IR pulses temporally delayed to each other, we design an incident pulse polarization control method on the THG sideband lasers and also acquire the low-frequency surface Raman spectrum of the amorphous medium.   © 2013 Optical Society of America

OCIS codes: (190.2620) Harmonic generation and mixing; (260.7190) Ultraviolet; (320.2250) Femtosecond phenomena; (320.7110) Ultrafast nonlinear optics; (190.4380) Nonlinear optics, four-wave mixing.
http://dx.doi.org/10.1364/OL.38.003304

Light conversion in nonlinear materials is an active and fruitful research field [1]. Besides numerous reports on second-harmonic generation in anisotropic media, the intriguing phenomenon of third-harmonic generation (THG) at interfaces under tight focusing conditions has been explored [2–7]. Ideally, molecular-level structural and dynamics information can be retrieved from THG photons that are observed in almost all optical media. When an interface is present within the focal volume of the excitation beam, THG is allowed on the basis of an effective third-order surface nonlinear susceptibility, and the generated surface THG is much stronger than that in bulk materials. To date, most studies on interface THG have been focused on the characterization of ultrafast pulses by autocorrelation and frequency-resolved optical-gating techniques [8,9], study of interface low-frequency Raman modes of crystals in a microscopic system [10,11], and optical imaging [12,13]. The application potential of these THG signals, however, is limited by the information retrievable from a single ultraviolet (UV) signal output of an optical setup involving an oscillator pulse on crystals.

In this Letter, we report a new optical phenomenon of concomitantly generating three distinct sets of broadband THG signals from two noncollinear 800 nm amplified fundamental pulses (FPs), tightly focused onto a thin amorphous borosilicate (BK7) glass slide. The UV signals emerge at the glass–air interface via direct third-order $[\chi^{(3)}]$ as well as cascaded third-order $[\chi^{(3)}:\chi^{(3)}]$ nonlinear processes. First, the THG signals $TH_{FP1,2}$ that are collinear with the FPs (see Fig. 1) are individually formed by each FP. Second, the THG signals $TH_{\pm1}$ are generated by noncollinear interactions between two FPs. Third, the novel THG signals $CTH_{\pm1}$ arise from interactions between the FPs and the nascent cascaded four-wave mixing (CFWM) sidebands. The simultaneous observation of multiple THG signals via different mechanisms is rooted in our compact and versatile setup, mainly consisting of one thin nonlinear medium and two incident amplified near-IR pulses in a crossing geometry. We characterize the $TH_{\pm1}$ signals spectrally and temporally, and

implement a new incident beam polarization control of the THG output. Upon varying the time delay between the two intense FPs, we obtain the low-frequency surface Raman spectrum of an amorphous medium (e.g., fused silica) from the ultrafast oscillatory component of the THG signal intensity temporal profile, which is further supported by our femtosecond stimulated Raman spectroscopy (FSRS) measurements on the same material [14].

The experiment is performed using a femtosecond (fs) mode-locked Ti:sapphire regenerative laser amplifier (Legend Elite, Coherent) that provides a 35 fs pulse train centered at 800 nm with a 1 kHz repetition rate. The FP with ~50 µJ/pulse energy is separated by a 50/50 beam splitter; both arms are then attenuated by an iris and a variable neutral density filter to ~8 µJ/pulse. The two p-polarized FPs are tightly focused onto a 0.15-mm-thick BK7 glass slide using an $f = 100$ mm spherical concave mirror. The laser focal diameters on the glass back surface are ~0.2 mm with a crossing angle of ~6°.
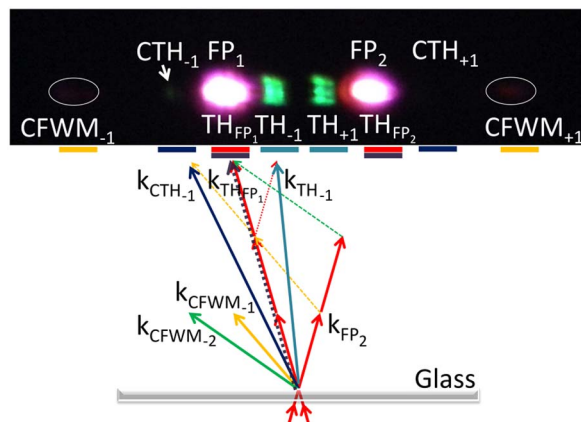

Fig. 1.   Photograph of THG and CFWM sideband signals with FP power of ~8 µJ/pulse. The relatively dim CFWM sidebands in the near IR are highlighted by the white circles. The different sets of distinct sideband pulses are labeled. Bottom, wave vector diagrams illustrating the various phase-matching conditions responsible for the nascent THG and CFWM sideband lasers.

The steady-state spectra and kinetic traces of THG signals are measured by a spectrograph with a 600 grooves/mm, 400 nm blaze reflective grating and a front-illuminated CCD camera (PIXIS: 100F, Princeton Instruments) calibrated by an Hg–Ar standard source. The FPs and CFWM signals in the near IR are recorded by a spectrometer (Ocean Optics). For time-resolved measurement, one FP passes through a motorized delay stage (CVI Melles Griot 07EAS504) and a phase-locked optical chopper; transient dynamics of each sideband signal can thus be isolated, dispersed, and characterized. FSRS is exploited to capture the low-frequency Raman spectrum of a thin fused silica window, with the detailed setup reported in our previous work [14]. In brief, the fundamental laser with ~1.6 mJ/pulse energy is dispersed by a ruled reflective grating (1200 grooves/mm, 750 nm blaze) and passed through an adjustable slit with ~90 μm width corresponding to the Raman pump bandwidth of ~10 cm^{-1} and pulse duration of ~3.5 ps. To achieve an ultrabroad detection window of ca. 100–4000 cm^{-1}, the Raman probe is selected from a CFWM sideband array generated by two crossing weak near-IR pulses in another 0.15-mm-thick BK7 glass slide [15]. The Raman pump and probe beams are focused onto the sample using a parabolic mirror. After transmission, the probe beam carrying the stimulated Raman signal is recollimated and focused into a spectrograph, followed by dispersion and imaging onto the CCD array camera.

We previously demonstrated that when an FP and a weak supercontinuum white light are noncollinearly focused onto a thin nonlinear crystal or an amorphous medium, the versatile broadband upconverted multicolor arrays emerge from the CFWM processes [16,17]. In the present work, when two intense FPs (~8 μJ/pulse, ~35 fs pulse width, ~7 × 10^{11} W/cm^2 peak power density that is well below the damage threshold for glass [18]) are temporally and spatially overlapped as well as tightly focused on the back surface of a thin glass slide, a series of spatially dispersed sideband signals emerge between and beside the two FP beams shown by the photograph in Fig. 1. Note that the UV signals appear in pairs due to the symmetric geometry of the two equivalent FPs. Figure 2 presents the normalized spectra of all the

sidebands along with the FPs. Two pairs of near-IR pulses (CFWM$_{\pm1,2}$ in Fig. 1) are observed, and based on the phase-matching condition (PMC) depicted, it can be assigned to CFWM processes via two interacting FPs [16,19]. Moreover, three distinct pairs of UV pulses are observed near the FPs and imaged using a fluorescence card and a UV bandpass filter. When a laser beam is tightly focused on a medium, the THG processes are found to be weak inside the bulk owing to Gouy phase shift, which induces destructive interference and consequently cancels THG [2,5]. However, this effect is dramatically suppressed at the interface and THG signals can be much enhanced [5,6]. In our setup, because the thin BK7 glass is transparent at the FP wavelength range but strongly absorbs in the UV, the observed THG signals can only originate from the back surface of the glass that faces the air. As illustrated in Fig. 1, three pairs of THG signals with distinct center wavelengths are obtained via different PMC mechanisms. The TH$_{FP1,2}$ sidebands at 265 nm propagating collinearly with FPs are directly generated by each FP at the glass–air interface [6], i.e., $\omega_{TH\_FP1,2} = 3\omega_{FP1,2}$ where $\omega_{TH\_FP1,2}$ and $\omega_{FP1,2}$ are frequencies of TH$_{FP1,2}$ and FP$_{1,2}$, respectively. The most pronounced UV signals TH$_{\pm1}$ at 267 nm appear in between the two crossing FPs, e.g., $\omega_{TH-1} = 2\omega_{FP1} + \omega_{FP2}$. The newly identified weak CTH$_{\pm1}$ signals at 263 nm are associated with the cascaded processes based on pure third-order susceptibility $[\chi^{(3)}:\chi^{(3)}]$ via coupling between the FPs and the nascent first-order CFWM$_{\pm1}$ signals, e.g., $\omega_{CTH-1} = 2\omega_{FP1} + \omega_{CFWM-1}$ while $\omega_{CFWM-1} = 2\omega_{FP1} - \omega_{FP2}$. All the UV signals have an ultrabroad bandwidth of ~1450 cm^{-1}. We remark that the observation of all the laser sidebands requires them to fulfill both the energy and wave vector conservation equations. Considering the noncollinear copropagation of the two incident FPs, the crossing-angle-dependent PMC [16,19] for THG signals demonstrates a similar trend of center wavelength variation as compared with the spectra in Fig. 2, e.g., the cascaded CTH signals are blueshifted from other noncascaded THG signals.

Figure 3 displays the ultrafast nonresonant dynamics of the observed THG and CFWM signals. The delay-time-dependent traces manifest different temporal responses due to varied PMCs for distinct cubic processes. For TH$_{\pm1}$ signals [Fig. 3(a)], assuming Gaussian pulse shape, the fitting yields an ~36 fs incident pulse width that matches the FP duration [20]. In practice, THG at the glass–air interface is an efficient method to diagnose fs pulses [8,9] independent of laser wavelength and requiring much less stringent phase matching as compared to second-order nonlinear pulse characterization methods [5]. CFWM$_{\pm1}$ signals [Fig. 3(b)] stem from phase matching of cascaded processes inside the bulk glass, and the temporal profile is fitted with a Gaussian corresponding to ~48 fs incident pulse duration. The dynamics is derived from the ~100 fs electronic response time of bulk glass [21], hence giving a broader time-dependent intensity profile compared to TH$_{\pm1}$ signals. For CTH$_{\pm1}$ signals [Fig. 3(c)], the cascaded coupling between the FPs and CFWM$_{\pm1}$ signals leads to an even broader temporal profile, indicating a pulse duration of ~69 fs. The TH$_{FP}$ signals [Fig. 3(d)] are generated by individual
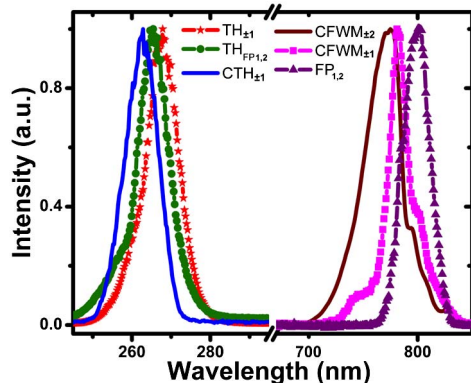

Fig. 2. Normalized spectra of the newly generated THG and CFWM sidebands using two intense fs FP laser beams tightly focused onto a 0.15-mm-thick BK7 glass slide. The spectral shift of the nascent THG sidebands in the UV as well as the CFWM sidebands in the near IR wavelength range is apparent.
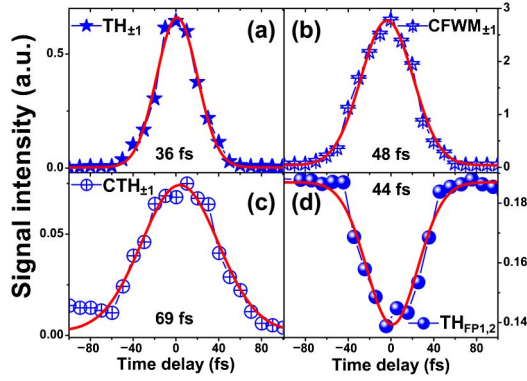
Fig. 3. Ultrafast temporal profiles of the signal intensities for (a) $TH_{\pm 1}$, (b) $CFWM_{\pm 1}$, (c) $CTH_{\pm 1}$, and (d) $TH_{FP1,2}$ sideband signals. The solid curves represent the Gaussian-profile fitting results. The corresponding incident pulse width in real time with a typical Gaussian shape is computed (based on the FWHM ratio of 1.225 for THG) and listed in each subfigure for comparison. The relative signal strength is reflected by the integrated peak intensity on CCD, e.g., $CTH_{\pm 1}$ is much weaker than $CFWM_{\pm 1}$.
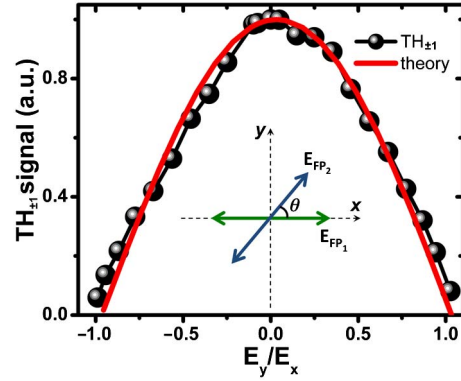

Fig. 4. Composite polarization state dependence of $TH_{\pm 1}$ sideband signals generated at the glass–air interface upon varying the crossing angle θ between the two depicted FP polarizations. Multiple runs of tuning the θ values between 0 and $\pm \pi/2$ are performed to ensure reproducibility, and the averaged $TH_{\pm 1}$ signal intensity at each θ is plotted against the y/x electric field amplitude ratio therein. The smooth solid curve represents the theoretical calculation (see text).

FPs, and their temporal response manifests a negative dip with a correlative pulse duration of ~44 fs due to FP energy loss for generating the aforementioned other THG and CFWM signals. The energy conversion efficiency of all the sidebands is ~6% due to $\chi^{(3)}$ processes measured by the FP power past the glass slide with and without the interaction of the other FP beam. This effect can be qualitatively seen from the loss of $TH_{FP1,2}$ signals.

The discovery of such an array of multiple THG laser sidebands in a thin medium prompts us to explore their practical application besides measuring the incident pulse duration. It was established that a circularly polarized laser beam could not produce THG radiation in isotropic materials [2,6]. In particular, the dependence of THG on the polarization and ellipticity of the driving fields was reported by Tsang [6], wherein the incoming beam ellipticity was tuned by rotating a $\lambda/4$ wave plate placed before the focusing lens for THG. The beam ellipticity was defined as the ratio of the two axes of the polarization ellipse ($\varepsilon = E_y/E_x$), which could be consecutively tuned from 0 (linear) to 1 (circular polarization) and hence dramatically control the THG output. In our experiment, we implement a new design: by simply rotating the polarization of one of the two incoming FPs via a $\lambda/2$ wave plate, both FPs are still linearly polarized but with a crossing angle θ between their polarized directions. The electric field amplitudes of the two axial components for the composite polarization state can thus be expressed as $E_x = [E_{FP1}^2 + (E_{FP2} * \cos \theta)^2]^{1/2}$, and $E_y = E_{FP2} * \sin \theta$, where $E_{FP1,2}$ is the electric field strength of the two linearly polarized FPs. In other words, our two-FP linear polarization crossing geometry imitates the one-pulse elliptic polarization state. As θ is tuned from 0 to $\pm \pi/2$ by rotating the $\lambda/2$ wave plate in the FP_2 beam path, the $TH_{\pm 1}$ signals are switched off simultaneously, confirming that both FPs participate in generating these UV signals sandwiched between them (see Fig. 1). The experimental and theoretical results for FP-polarization-dependent $TH_{\pm 1}$ signal are presented in Fig. 4. The THG signal versus ε exhibits the general

bell-shape response [6] and matches very well with the calculated values based on the expression $\cos(\varepsilon \pi/2)$ shown as the smooth solid curve in Fig. 4. In contrast to a previous report using a sophisticated spatial light modulator to manipulate polarization and enhance THG imaging spatial resolution [22], this newly observed THG dependence on a composite polarization state paves a convenient way for further incorporating a third FP (e.g., twice as strong as the first two FPs) to achieve all optical switch [23] for the spatially separated UV signal (e.g., $TH_{\pm 1}$) on the fs timescale.

A close inspection of the UV signal intensity profile upon delaying one of the FPs reveals fs quantum beating. It has been reported by Bartels and coworkers [11,24] that the vibrational motion in noncentrosymmetric crystals can be resolved by studying the THG signal at the crystal–air interface. We tackle the problem using amorphous glass that is centrosymmetric and observe a reproducible time-resolved oscillation in the background-free $TH_{\pm 1}$ kinetic trace (i.e., not the dynamics of the two FPs in a typical pump-probe setup). At the same experimental
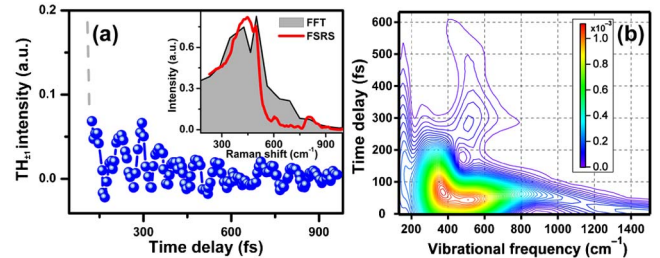

Fig. 5. (a) Ultrafast dynamics of the $TH_{\pm 1}$ sideband signal intensity collected from a thin fused silica slide. The inset shows the low-frequency Raman modes of fused silica from FFT of the $TH_{\pm 1}$ temporally oscillatory intensity trace, in comparison with the Stokes–Raman spectrum from our FSRS experiment on the same material. (b) Time-frequency-domain results of the $TH_{\pm 1}$ dynamics through wavelet decomposition using Morlet wavelet basis. The distinct time evolution of the two dominant coherent Raman modes below 600 cm^{-1} on the subpicosecond time scale is salient.

condition with BK7 glass, Fig. 5(a) displays the ultrafast temporal response of $TH_{\pm 1}$ signals generated in a thin fused silica plate with the time delay step of ~6.7 fs. The modulating vibrational modes initiated by impulsive stimulated Raman scattering are retrieved by fast Fourier transform (FFT). The FP has an ~32 nm bandwidth, corresponding to coherent mode excitation up to ~500 cm^{-1}. For comparison, we collect the low-frequency Raman spectrum of pristine fused silica using a home-built FSRS setup with a newly improved CFWM-based probe [14,15], and the resulting spectrum is in excellent agreement with the literature [Fig. 5(a) inset]. The FFT spectrum shows a broad dominant band at ~440 cm^{-1}, attributed to the Si-O-Si bond rocking and bending in the noncrystalline matrix, generally six-membered rings of SiO_4 tetrahedra. The narrow band at ~500 cm^{-1} is assigned to four-membered rings in the largely random silica network. Using continuous Morlet wavelet basis to perform time-frequency domain analysis [25], we unravel the time evolution of each vibrational component detected. The lifetime of the Raman mode at ~440 cm^{-1} is ~200 fs [Fig. 5(b)], in accordance with the short-range optical phonon mode propagation in amorphous glass [26]. In contrast, the sharp feature at ~500 cm^{-1} diminishes after ~600 fs, implying a reduced mode inhomogeneity with longer-range ordering, consistent with the proposed higher density ring structure [27] and larger coherence interaction length in the condensed phase. The use of amplified fs pulses affords the opportunity to generate multiple UV sidebands, probe molecular properties *in situ*, and at the same time initiate photoinduced changes or interfacial chemical reactions. The incident-FP-power-dependent THG revealing laser-induced-crystallization on the glass surface will be reported in a future publication.

In summary, we report multiple THG signals being generated at the glass–air interface by tightly focusing two intense near-IR fs pulses onto a 0.15-mm-thick BK7 glass slide. Three distinct pairs of THG sidebands originate from nonlinear interactions between incident FP beams and their generated CFWM signals. It is notable that the cascaded THG signals ($CTH_{\pm 1}$) in our noncollinear setup arise from a different process from the previously reported cascaded second-order nonlinearity [$\chi^{(2)}$:$\chi^{(2)}$]-induced THG [3]. The CTH generation is recently demonstrated in our laboratory under similar experimental conditions for a wide range of nonlinear materials, including thin isotropic and anisotropic media (e.g., sapphire, BBO crystal) and liquid thin films (e.g., water). The UV signals can be switched off as the two incident FP polarizations become perpendicular to each other. Finally, by analyzing the background-free coherence-modulated $TH_{\pm 1}$ signals, we observe optical phonon oscillation dynamics from the back surface of fused silica. FFT and Morlet wavelet transfer results clearly resolve the dominant coherent low-frequency Raman modes of the amorphous material traversing the focal point of the two FPs. The generation and characterization of the ultrafast, spatially dispersed, mechanistically

diverse THG laser sidebands thus provide a viable and comprehensive new toolset to probe interface molecular properties of almost any thin nonlinear medium with high specificity, particularly for those amorphous materials lacking second-order nonlinearity.

References

1. R. W. Boyd, *Nonlinear Optics*, 3rd ed. (Academic, 2008).
2. W. K. Burns and N. Bloembergen, Phys. Rev. B **4**, 3437 (1971).
3. G. R. Meredith, Phys. Rev. B **24**, 5522 (1981).
4. B. Buchalter and G. R. Meredith, Appl. Opt. **21**, 3221 (1982).
5. T. Y. F. Tsang, Phys. Rev. A **52**, 4116 (1995).
6. T. Tsang, Phys. Rev. A **54**, 5454 (1996).
7. C. Bosshard, U. Gubler, P. Kaatz, W. Mazerant, and U. Meier, Phys. Rev. B **61**, 10688 (2000).
8. T. Tsang, M. A. Krumbugel, K. W. DeLong, D. N. Fittinghoff, and R. Trebino, Opt. Lett. **21**, 1381 (1996).
9. S. K. Das, C. Schwanke, A. Pfuch, W. Seeber, M. Bock, G. Steinmeyer, T. Elsaesser, and R. Grunwald, Opt. Express **19**, 16985 (2011).
10. D. Kupka, J. W. Wilson, O. Masihzadeh, and R. A. Bartels, Chem. Phys. Lett. **490**, 97 (2010).
11. J. W. Wilson and R. A. Bartels, J. Opt. Soc. Am. B **29**, 1875 (2012).
12. J. Squier, M. Muller, G. J. Brakenhoff, and K. R. Wilson, Opt. Express **3**, 315 (1998).
13. D. Debarre, W. Supatto, A.-M. Pena, A. Fabre, T. Tordjmann, L. Combettes, M.-C. Schanne-Klein, and E. Beaurepaire, Nat. Methods **3**, 47 (2006).
14. W. Liu, F. Han, C. Smith, and C. Fang, J. Phys. Chem. B **116**, 10535 (2012).
15. L. Zhu, W. Liu, and C. Fang, Appl. Phys. Lett. **103**, 061110 (2013).
16. W. Liu, L. Zhu, and C. Fang, Opt. Lett. **37**, 3783 (2012).
17. W. Liu, L. Zhu, L. Wang, and C. Fang, Opt. Lett. **38**, 1772 (2013).
18. A.-C. Tien, S. Backus, H. Kapteyn, M. Murnane, and G. Mourou, Phys. Rev. Lett. **82**, 3883 (1999).
19. H. Crespo, J. T. Mendonca, and A. Dos Santos, Opt. Lett. **25**, 829 (2000).
20. Y. Miyoshi, S. Zaitsu, and T. Imasaka, Appl. Phys. B **103**, 789 (2011).
21. J. E. Aber, M. C. Newstein, and B. A. Garetz, J. Opt. Soc. Am. B **17**, 120 (2000).
22. O. Masihzadeh, P. Schlup, and R. A. Bartels, Opt. Lett. **34**, 1240 (2009).
23. T. Volz, A. Reinhard, M. Winger, A. Badolato, K. J. Hennessy, E. L. Hu, and A. Imamoglu, Nat. Photonics **6**, 605 (2012).
24. J. W. Wilson, P. Schlup, and R. Bartels, Opt. Lett. **33**, 2116 (2008).
25. C. Chatfield, *The Analysis of Time Series: An Introduction*, 6th ed. (Chapman & Hall/CRC, 2004).
26. S. Li, H. Huang, W. Zhu, W. Wang, K. Chen, D.-x. Yao, Y. Wang, T. Lai, Y. Wu, and F. Gan, J. Appl. Phys. **110**, 053523 (2011).
27. J. W. Chan, T. Huser, S. Risbud, and D. M. Krol, Opt. Lett. **26**, 1726 (2001).